Deformation mechanisms in single crystal Ni-based concentrated solid solution alloys by nanoindentation

Liuqing Yang[1], Youxing Chen[1,2,*], Jimmie Miller[1], William J. Weber[3], Hongbin Bei[4], Yanwen Zhang[3,5,*]

[1] Department of Mechanical Engineering and Engineering Science, University of North Carolina at Charlotte, Charlotte, NC 28223, United States

[2] Energy Production & Infrastructure Center, University of North Carolina at Charlotte, Charlotte, NC 28223, United States

[3] Department of Materials Science & Engineering, University of Tennessee, Knoxville, TN 37996, United States

[4] School of Materials Science and Engineering, Zhejiang University, Hangzhou 310027, China

[5] Materials Science and Technology Division, Oak Ridge National Laboratory, Oak Ridge, TN 37831, United States

Abstracts

Nanoindentation is a critical technique to probe mechanical properties at the micrometer and sub-micrometer scales, accompanied by challenges from indentation size effect, pile-up/sink-in effect, and strain rate sensitivity. In this study, different nanoindentation techniques have been employed to explore Ni-based concentrated solid solution alloys (CSAs) with the addition of 3*d* transition metal elements including Co, Cr, Mn, and Fe, including unique single-crystal Ni, NiCo, NiFe, $Ni_{80}Cr_{20}$, and NiCoFeCr samples with (100) surfaces. A procedure of nanoindentation tests and data analysis/correction have been developed, and a data set of hardness, elastic modulus, strain rate sensitivity, and activation volume for Ni-based CSAs are provided, including the less explored binary alloys such as $Ni_{80}Cr_{20}$ and $Ni_{80}Mn_{20}$. The results show that the type of alloying elements is more critical than the number of elements in strengthening: Co does not provide strengthening in NiCo, while Cr, Mn, and Fe are effective strengthening elements. Cr is the most effective among all the 3*d* transition metal elements. Furthermore, atomic-level lattice distortion is responsible for the strengthening and the role of stacking fault energy is insignificant in Ni-based CSAs at room temperature. In summary, nanoindentation shows increasing promise as a reliable and fast tool to provide comprehensive mechanical information for new alloy design and development.

* Corresponding authors: Y.Chen ychen103@uncc.edu; Y.W. Zhang zhangy1@ornl.gov

List of Acronyms and Abbreviations

AFM	Atomic Force Microscope
BCC	Body-Centered Cubic
CCA	Complex, Concentrated Alloy
CSA	Concentrated Solid-solution Alloy
CSM	Continuous Stiffness Measurement
FCC	Face-Centered Cubic
FIB	Focus Ion Beam
GND	Geometrically Necessary Dislocation
HEA	High Entropy Alloy
ISE	Indentation Size Effect
MPEA	Multi-Principal Element Alloy
SAD	Selected-Area Diffraction
SFE	Stacking Fault Energy
SRO	Short-Range Order
SSD	Statistically Stored Dislocation
TEM	Transmission Electron Microscopy
A	Geometrical Contact Area
A_c	Corrected Contact Area
A_{pu}	Pile-up Area
a_i	Contact periphery of the indenter
b	Edge Length of Residual Imprint
$\boldsymbol{b}$	Burgers Vector
c_i	Atomic Percentage of Component
E	Elastic Modulus
h	Penetration Depth
h^*	Characteristic Depth
h_i	Height of pile-up
H	Nanoindentation Hardness
$\dot{H}$	Hardness Change Rate
H_0	Macro-hardness
H_{0_C}	Pile-up Corrected H_0
H_{IT}	Nanoindentation Hardness
H_{IT_C}	Pile-up Corrected H_{IT}
$\dot{h}$	Displacement Rate

h	Instantaneous Displacement
l	Length of Dislocation Segment
m	Strain Rate Sensitivity
M	Taylor Factor
P	Load
$\dot{P}$	Loading Rate
r_i	Atomic Radius of Component
T	Absolute Temperature
V	Activation Volume
V_f	Activation Volume of Forest Hardening
V_{SS}	Activation Volume of Solid Solution Strengthening
V_n	Atomic Volume
w	Distance of Overcoming Energy Barrier
α	Dislocation Line Tension Parameter
γ	Average Shear Strain
ΔE_b	Total Energy Barrier
$\Delta\bar{V}_n$	Average Misfit Volume
δ	Lattice Distortion
δ_G	Lattice Distortion Calculated Using Goldschmidt Radius
δ_{rlx}	Lattice Distortion Calculated from Relaxed Structure
$\dot{\varepsilon}_\iota$	Strain Rate for Nanoindentation
κ	Boltzmann Constant
μ	Shear Modulus
ρ_G	Density of Geometrically Necessary Dislocation
ρ_S	Density of Statistically Stored Dislocation
σ	Stress
σ_Y	Yield Strength
σ_{UTS}	Ultimate Tensile Strength
σ_{ss}	Solid Solution-induced Strength
τ_{y0}	Zero-temperature Flow Stress

1. Introduction

A new class of alloys containing multiple elements in near-equiatomic concentrations was reported by two groups [1, 2] independently in 2004. In contrast to conventional alloys with a limited number of possible element combinations because of the tendency to cluster around the corners or edges of phase diagrams, these new alloys near the centers of phase diagrams provide significantly more element combinations, especially in quaternary, quinary and higher-order systems. Yeh and co-workers proposed a new name, high entropy alloys (HEAs), for this new class of alloys containing five or more elements in relatively high concentrations (5–35 at.%). They reasoned that, as the number of elements in an alloy increased, the entropic contribution to the total free energy would overcome the enthalpic contribution and stabilize solid solutions. The concept of HEA has created a wave of research to explore the extended materials design space for mechanical properties [3-5] and radiation tolerance [6-8] that were hitherto thought to be unobtainable. Some alternative names with extended concepts were also used in literature, such as multi-principal element alloys (MPEAs), complex, concentrated alloys (CCAs) [9], and concentrated solid solution alloys (CSAs) [8]. As discussed in [6], entropic stabilization is not predominant or is overturned, nevertheless, the HEA concept has also inspired a re-evaluation of classical thermodynamic concepts as they apply to CSAs [9]. In this study, the name of CSAs is adopted, including binary and quaternary alloys.

The benchmark material, single-phase equiatomic CrMnFeCoNi "Cantor" alloy, demonstrates a break-up of the strength-ductility trade-off. The investigation of this alloy laid the foundation for the fundamental understanding of HEAs [3, 6, 10]. Later, it was discovered that besides configurational entropy (i.e., the number of alloying elements), the nature of the constituent elements also significantly affects mechanical properties [11]. For example, alloys with the same number of elements may show different mechanical strengths [11]: Quaternary FeNiCoCr is much stronger than FeNiCoMn; Ternary CrCoNi is much stronger than MnFeNi; Binary FeNi is much stronger than NiCo. In addition, the ternary CrCoNi alloy has a higher strength than the quinary CrMnFeCoNi alloy and quaternary FeNiCoCr, NiCoCrMn, and FeNiCoMn alloys [11]. These surprising findings have triggered more generalized studies on CSAs with multiple principal elements.

The unique feature of atomic-level complexity [12, 13] in CSAs results in lowered and varying stacking fault energies (SFEs), atomic volume misfit and short-range order (SRO), which modify dislocation behavior (e.g., friction stress) and twinning activities. The fundamental plasticity mechanisms in CSAs such as dislocation nucleation/ propagation, dislocation-obstacle interaction, phase transformation and twinning are similar to those in conventional alloys [3, 4]. Therefore, many studies are devoted to incorporating the unique features of CSAs, such as lattice distortion, SRO, entropy, and sluggish diffusion, to the classic theories used for conventional alloys with only one principal element [3]. For instance, for high-entropy CrMnFeCoNi, a combination of high strength, great work hardening, and excellent ductility was ascribed to a synergy of multiple deformation mechanisms, including the easy motion of Shockley partial dislocations, dislocation interactions to form stacking-fault parallelepipeds, and dislocation arrest at planar slip bands of undissociated dislocations [14]; For medium-entropy CrCoNi, Laplanche *et al.* ascribed high strength and good ductility to nanoscale twinning [15] and Zhang *et al.* ascribed strength-ductility synergy of CrCoNi to localized face-centered cubic (FCC) – body-centered cubic (BCC) phase transitions due to SRO prior to the ultimate stress [16]; Wu *et al.* compared tensile properties of

single-phase binary, ternary and quaternary CSAs at different temperatures and emphasized the critical role of constituent elements [11].

First-principles calculations have been used to study the origin of these unique features of CSAs. The key to bridging local electronic structure features and mechanical behaviors is to understand the behavior of deformation-associated defects in CSAs [17], such as dislocations and twins. For example, Zhao *et al.* discovered that in FCC CSAs, the variation of SFE is related to the electronic properties of the constituent elements, while its temperature dependence is governed by phonon properties [18]. Recently, it was reported that solid solution strengthening in FCC CSAs is ascribed to the configurational fluctuation of the atomic-level pressure originating from the charge transfer between neighboring elements [12]. However, this strengthening model overestimates the strength by a factor of four compared to the experimental results. Therefore, more delicate and robust descriptors are still needed to quantitatively describe the mechanical behaviors of CSAs from the perspective of the local electronic structure features [17, 19].

Hardness is widely used and technically relevant property of materials. As stated by Tabor [20], "hardness implies the resistance to deformation" and "the indentation hardness of metals may in general be expressed in terms of the plastic and, to a lesser extent, the elastic properties of the metals concerned". Since the Brinell test was invented in the 1900s, various macro-/ micro-indentation tests and corresponding ASTM standards have been developed. For instance, ASTM E10, E18 and E92 have been used for Brinell, Rockwell, and Vickers tests of metallic materials, respectively.

To meet ever-increasing needs and interests in predicting material behaviors in the world of the small, nanoindentation is a critical technique to probe mechanical properties at the micrometer and sub-micrometer scales. It benefited from the development of instruments capable of continuously measuring load and displacement throughout an indentation [21, 22]. Nanoindentation has the advantage of easy sample preparation and statistically rich data sets [22, 23]. This technique is especially important for thin films [24-26] and surface-modified materials (e.g., ion-irradiated materials [27-31]), of which the mechanical property measurement cannot be achieved by traditional mechanical tests (e.g., tensile tests) due to limited volume. The methods and applications have been recently reviewed [32-34].

Hardness and elastic modulus are the two most common properties obtained from nanoindentation. The hardness is usually defined as the ratio of the indentation load and either the surface or projected area of residual indents, in which the indentation load underneath the tip depends on elastic modulus, yield strength, Poisson's ratio, work-hardening exponent, and indenter geometry [35, 36]. Essentially, the hardness represents a flow state of materials underneath the indenter: Tabor [37] pointed out that the hardness is approximately 3 times the yield strength (σ_Y) for materials without work-hardening behavior; For fully hardened materials, the hardness is approximately 3 times the ultimate tensile strength (σ_{UTS}). Most metallic materials have hardness values between $3\sigma_Y$ and $3\sigma_{UTS}$. Tabor [37] also noted that bulk indentation hardness is approximately 3 times the flow stress at a representative strain of 8% - 10%. A detailed discussion of different types of relationships between hardness and strength is reported elsewhere [35]. A recent study showed that single-phase HEAs conform to the 3-times relation between Vickers hardness and σ_{UTS} [38]. However, size and scale effects for smaller sample dimension or volume have been observed in numerous studies and are critical to not only understand the new phenomena at the smaller scale but also quantitatively correlate materials behavior at this scale to that at a

larger scale, such as in micro/macro-indentation and uniaxial tension. The influence of factors such as pile-ups/sink-ins and indentation size effects (ISE) needs to be considered [39].

More comprehensive material properties collected by nanoindentation techniques are required to accelerate the screening/investigation of new advanced alloys. In this study, Ni-based CSAs with the addition of 3*d* transition metal elements including Co, Cr, Mn, and Fe are the focus as these elements have shown effective modification of electron band structure and promising property improvement. The study is more comprehensive than previous studies on Ni-based CSAs for several aspects: (a) it includes unique single-crystal Ni, NiCo, NiFe, $Ni_{80}Cr_{20}$, and NiCoFeCr samples with the same crystallographic orientation that exclude microstructural and grain orientation effects; (b) it investigates a broad spectrum of CSAs, including the less explored NiCr and NiMn binary alloys. A direct comparison of Ni, NiCo, NiFe, $Ni_{80}Cr_{20}$, $Ni_{80}Mn_{20}$, and NiCoFeCr is available for insights to future materials design; (c) it provides a thorough procedure of nanoindentation data correction for indentation hardness and strain rate sensitivities of Ni-based CSAs, which is important but not previously available in the literature [11].

The structure of this paper is as follows: First, hardness correction, including ISE and pile-ups in various CSAs is performed and discussed (3.1); Then, two types of deformation related dislocations that can assist in the understanding of deformation mechanisms under nanoindentation are calculated and compared, i.e., geometrically necessary dislocations and statistically stored dislocations (3.2); After that, the dislocation migration is discussed through the activation volume of dislocations in CSAs, which is calculated through strain rate sensitivity from nanoindentation strain rate jump tests with consideration of ISE (3.3); Finally, deformation mechanisms of CSAs including solid solution strengthening and forest hardening are discussed (3.4).

2. Materials & Methods

Ni-based single-phase CSAs, including pure Ni, binary Ni-based alloys [40, 41] ($Ni_{80}Cr_{20}$, $Ni_{80}Mn_{20}$ NiCo, NiFe with 20 at.% Cr, 20 at.% Mn, 50 at.% Co and 50 at.% Fe, respectively), and quaternary Ni-based alloy (NiCoFeCr) [42], were prepared by arc-melting. The atomic percentages were chosen based on phase stability to maintain an FCC crystal structure. For instance, 20 at.% Cr was selected in $Ni_{80}Cr_{20}$ due to the fact that FCC phase is not stable at 500°C once the Cr concentration exceeds 22 at.% [41, 43] according to the phase diagram. Similarly, 22% is the maximum Mn concentration for alloying Ni and Mn to form a stable FCC phase [41]. The purity of Ni, Fe, Cr, and Mn for arc melting is higher than 99.9%. The arc-melted buttons were flipped and re-melted at least five times before drop casting to ensure homogeneous mixing. A floating-zone directional solidification method was used for single-crystal growth.

The nanoindentation was performed on Agilent NanoIndenter G200 (MTS) with a Berkovich diamond tip. The continuous stiffness measurement (CSM) based on the Oliver-Pharr method [22] was chosen to record hardness and elastic modulus values as a function of penetration depth continuously. The tip area function was corrected on a fused silica sample. Eight indents were performed on each sample with a maximum penetration depth of 2 μm. In addition to standard hardness and elastic modulus measurement, strain rate sensitivity of samples was also obtained using nanoindentation strain rate jump testing technique. Three strain rates were selected: 0.05/s, 0.007/s and 0.001/s. As hardness decreases along with the depth, strain rate sensitivity was corrected to account for the hardness change rate (unit: Pa/s), which will be discussed later. To evaluate the amount of pile-ups around indents, an Atomic Force Microscope (AFM, Veeco Dimension 3100 Metrology AFM) was utilized to image indent topographies. AFM micrographs

were analyzed using Gwyddion software [44] and the correction method will be discussed later. The region underneath the indenter was lifted out by Focus Ion beam (FIB, model: FEI Quanta 3D workstation) and examined by Transmission Electron Microscopy (TEM, model: JEOL 2100).

3. Results and Discussion

Ni, NiCo, NiFe, $Ni_{80}Cr_{20}$, and NiCoFeCr were confirmed as single-crystal FCC structure with (100) surfaces in our previous studies [40-42], and $Ni_{80}Mn_{20}$ has a polycrystalline FCC structure with an average grain size of 100 – 200 μm [41], in which the grain boundary effects are negligible. The bright-field TEM micrographs of these materials are summarized in Fig. S1. After indentation, one indented region in the NiCo sample was lifted out by FIB and subsequently examined by TEM. The bright-field TEM micrograph (Fig. 1) of the indented region in NiCo shows the single-crystal feature. Bend contours and dislocation loops from indentation and FIB damage can be observed. The inset of the selected-area diffraction (SAD) pattern confirms that the NiCo sample has a single crystal FCC structure with (100) surface. No obvious subgrains were discovered in this indented region. Recently, electron backscatter diffraction and precession electron diffraction capable of mapping high-resolution crystallographic orientation revealed local crystal rotation near the indenter tip due to plasticity during nanoindentation [45, 46]. The orientation maps near the indenter for different Ni-based CSAs will be interesting to explore in the future, as they might suggest the difference in local plasticity in different Ni-based CSAs.

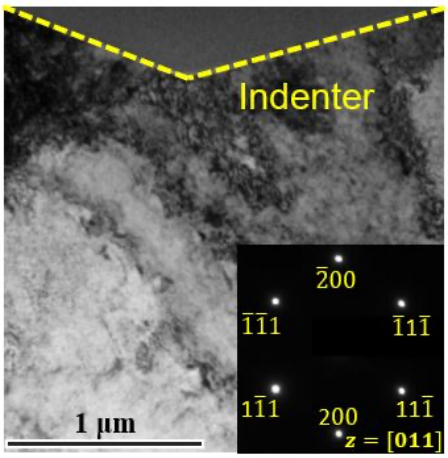

Figure 1. Bright-field TEM micrograph of the region underneath the indenter for NiCo. The inset of the selected-area diffraction pattern confirms the single-crystal structure after indentation and the surface normal of <100> crystallographic direction.

3.1 Nanoindentation hardness correction

Figure 2a compares hardness variation as a function of depth up to 2 μm. At a depth of 2 μm, Ni and NiCo have close hardness values of about 1.2 GPa; $Ni_{80}Cr_{20}$ shows the highest hardness of 2.2 GPa; $Ni_{80}Mn_{20}$, NiFe, NiCoFeCr show close hardness values of 1.8 GPa, 1.7 GPa, 1.9 GPa, respectively. The elastic moduli of Ni, NiCo, $Ni_{80}Mn_{20}$, $Ni_{80}Cr_{20}$, NiFe, and NiCoFeCr are 184±4, 174±6, 191±5, 205±3, 153±5, and 186±2 GPa, respectively. ISE is obvious for all samples in Fig. 2a, i.e., an increase in hardness with decreasing penetration depth [47]. To understand the ISE, the classic Nix-Gao model using the concept of geometrically necessary dislocations (GND) was followed [48], which describes the relationship between nanoindentation hardness (H) and macro-hardness (H_0) as

$$H = H_0\sqrt{1+\frac{h^*}{h}} \qquad (1)$$

where h represents penetration depth and $h^*$is defined as characteristic depth. Following Eqn. 1, H versus h curves in Fig. 2a were replotted as H^2 versus $1/h$ in Fig. 2b, in which H_0 and h^* can be obtained from the linear fitting: the intercept is H_0^2 and the slope is associated with the characteristic depth, h^*. The fitting range of 0.5 μm to 2 μm was selected to avoid the error from the blunt tip area. The intercepts and slopes for CSAs are summarized in Fig. 2c. For H_0, $Ni_{80}Cr_{20}$ is the hardest sample with a hardness value of 1.9 GPa, followed by $Ni_{80}Mn_{20}$, NiFe and NiCoFeCr with H_0 of 1.5-1.6 GPa. H_0 is lower for Ni (1.1 GPa) and NiCo (0.9 GPa) (Fig. 2a). NiCo has a stronger ISE than Ni. For comparison, the hardness at 2 μm without any correction is labeled as H_{IT} hereafter.

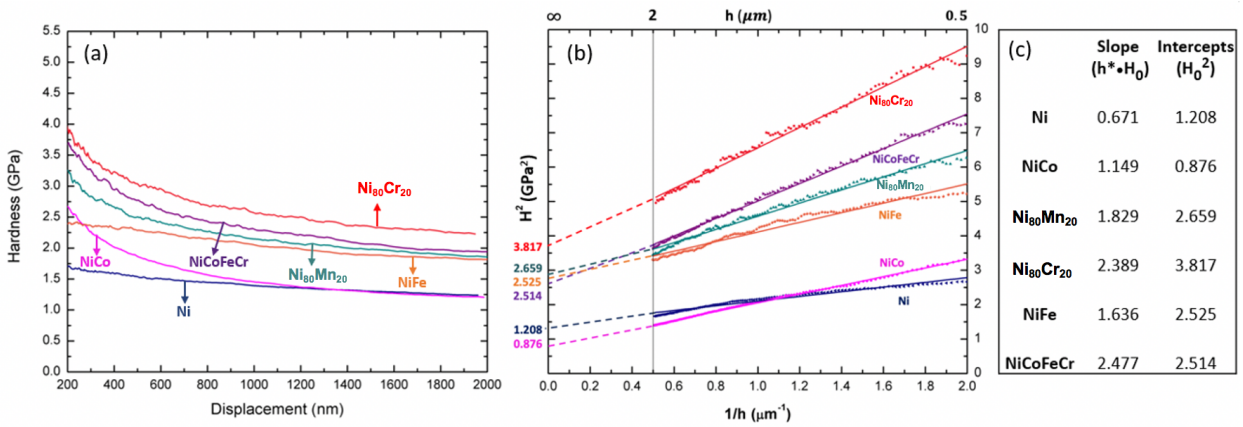

Figure 2. (a) A comparison of nanoindentation hardness (H) evolution of Ni, NiCo, $Ni_{80}Mn_{20}$, $Ni_{80}Cr_{20}$, NiFe and NiCoFeCr as a function of displacement (h, penetration depth); (b) a plot of H^2 vs. 1/ h with linear fitting on Ni and CSAs; (c) a summary of slopes and intercepts of fitting lines in (b).

In addition to ISE, pile-up/sink-in is another issue that underestimates/overestimates the contact area and therefore overestimates/underestimates the hardness. AFM micrographs (Fig. 3) of indentation imprints for Ni and CSAs demonstrate that pile-ups are obvious: qualitatively, pile-ups in Ni, $Ni_{80}Cr_{20}$ and NiFe are more obvious than those in $Ni_{80}Mn_{20}$, NiCo and NiCoFeCr. Quantitative pile-up corrections are discussed as follows.

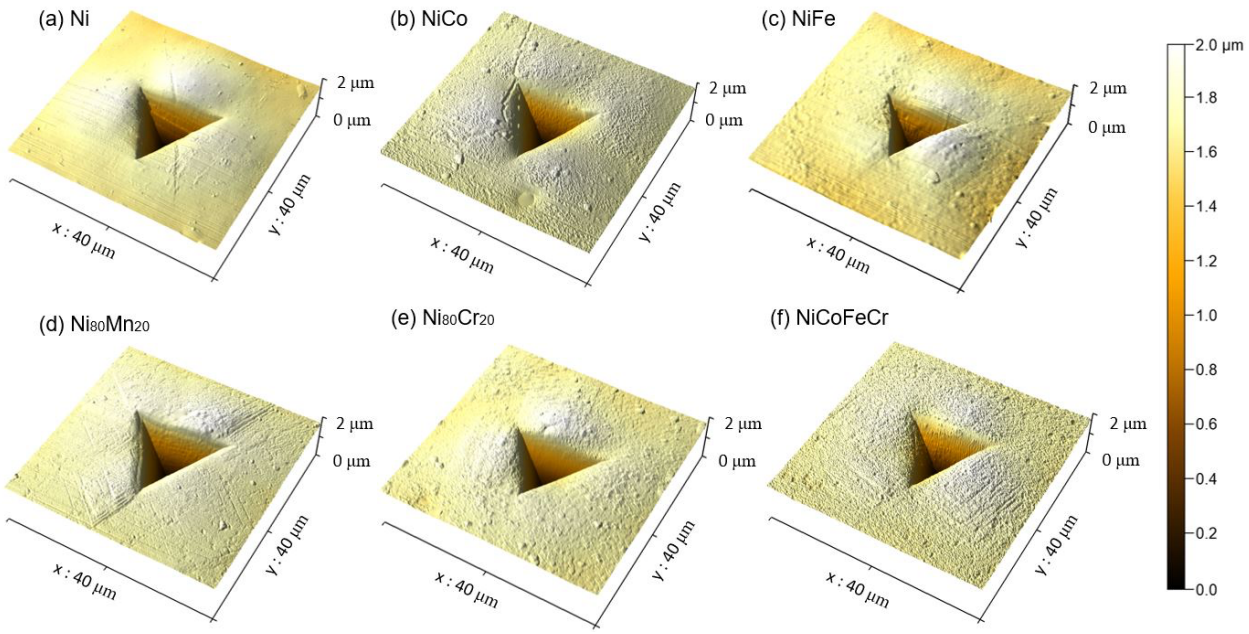

Figure 3. AFM micrographs of indentation imprints for Ni, NiCo, NiFe, $Ni_{80}Mn_{20}$, $Ni_{80}Cr_{20}$, and NiCoFeCr. Pile-ups exist in all samples.

There are several pile-up correction methods in the literature [49-51]. Kese's semi-ellipse method [52, 53] is employed in this study, as it is based on real surface morphology analysis near the imprints. Fig. 4a demonstrates an AFM micrograph of one representative pile-up in $Ni_{80}Cr_{20}$. Following Kese *et al*. [52], the corrected contact area (A_C) is composed of geometrical contact area (A) obtained from the Oliver and Pharr analysis of nanoindentation data and extra pile-up area (A_{pu}) as written as below,

$$A_C = A + A_{pu} \quad (2)$$

In this study, $A = 22.3852h^2 + 493.1381h$. A_{pu} is calculated as the sum of projection area along three edges following the work from Kese *et al*. [52]:

$$A_{pu} = \frac{\pi \mathrm{b}}{4} \sum a_i \quad (3)$$

where b was the edge length of the residual imprint of the Berkovich indenter characterized by AFM, a_i is the horizontal distance from the edge of the indent to the actual contact periphery (Fig. 4b).

Although this method of measuring a_i works well for high-strength and brittle materials, it introduces uncertainty when the pile-up peak is extended and broadened. As schematically shown in Fig. 4b, the usage of measured a_i is ideal (labeled as ideal) for calculating A_{pu} when the indenter tip is in contact with the peak of the profile. In such a case, a_i and h_i are correlated by $a_i = h_i \cdot tan65.3^{\circ}$ and the selection of either measured a_i or measured h_i for A_{pu} calculation is equivalent. However, if the pile-up extends further away, as schematically shown in Fig. 4b (labeled as real), A_{pu} is overestimated using the measured a_i for Eqn. 3. Surface profiles along three lobes in $Ni_{80}Cr_{20}$ (Fig. 4a) are shown in Fig. 4c and the pile-up region is magnified in Fig.

4d. When the Berkovich tip with three-fold rotational symmetry is in contact with (100) surface with four-fold rotational symmetry, the deformation near three sides is not equivalent and the pile-ups at three lobes are different: #1 (a_1=2.42 μm, h_1 = 0.26 μm); #2 (a_2=2.42 μm, h_2 = 0.20 μm) and #3 (a_2=4.68 μm; h_3 = 0.08 μm). It is noted that the selection of measured h_i for calculating A_{pu} is more reasonable than the selection of a_i based on three observations: (a) a_1 and a_2 are both equal to 2.42 μm, but their pile-up profiles are different; (b) #2 has a plateau, instead of a peak, and a_2 could vary from 2.42 μm to 3.93 μm (labeled as a_2' in Fig. 4d), which introduces a large uncertainty of A_{pu} calculation; (c) #3 has the largest a (a_3 = 4.68 μm), but the pile-up height (h_3=0.08 μm) is small and the profile shows a minimum pile-up. Therefore, A_{pu} for all indents is calculated using the measured h_i, and a_i is calculated by $h_i \cdot tan65.3^{\circ}$ for Eqn. 3.

With the calculated A_c/A (Ni: 1.17$\pm$0.02; NiCo: 1.13 $\pm$0.02; $Ni_{80}Mn_{20}$: 1.12 $\pm$0.02; $Ni_{80}Cr_{20}$: 1.16 $\pm$0.02; NiFe: 1.17 $\pm$0.01; NiCoFeCr: 1.13 $\pm$0.02), the hardness is corrected by:

$$\frac{A_c}{A} = \frac{H}{H_c} \quad (4)$$

The corrected hardness H_{IT} and macro-hardness H_0 (calculated from Nix-Gao model) are labeled as H_{IT_C} and H_{0_C}, and summarized in Fig. 5. The comparison of H_{IT}, H_{IT_C} and H_0 indicates that ISE and pile-up effect are the two major factors that cause the overestimation of hardness. It is interesting to note that whether ISE or pile-up effect is more dominant depends on the alloy compositions: pile-up effect plays a more dominant role in NiCo and NiCoFeCr.

Before the correction, the hardness values (H_{IT}) of Ni, NiCo, and NiFe are close to those reported in the literature [54]. After correction of the ISE and pile-up effects, H_{0_C} is the true macro-hardness values (Ni: 0.94 $\pm$ 0.08 GPa; NiCo: 0.83 $\pm$ 0.05 GPa; $Ni_{80}Mn_{20}$: 1.45 $\pm$ 0.01 GPa; $Ni_{80}Cr_{20}$: 1.65 $\pm$ 0.04 GPa; NiFe: 1.36 $\pm$ 0.02 GPa; NiCoFeCr: 1.40 $\pm$ 0.04 GPa). These alloys can be divided into two groups: Ni and NiCo have lower hardness of less than 1 GPa, while $Ni_{80}Cr_{20}$, $Ni_{80}Mn_{20}$, NiFe, NiCoFeCr have higher hardness of more than 1.35 GPa. $Ni_{80}Cr_{20}$ has the highest hardness. This suggests that Co does not have a strengthening effect. Mn, Cr, and Fe are effective elements in strengthening and Cr is the most effective, which will be discussed later.

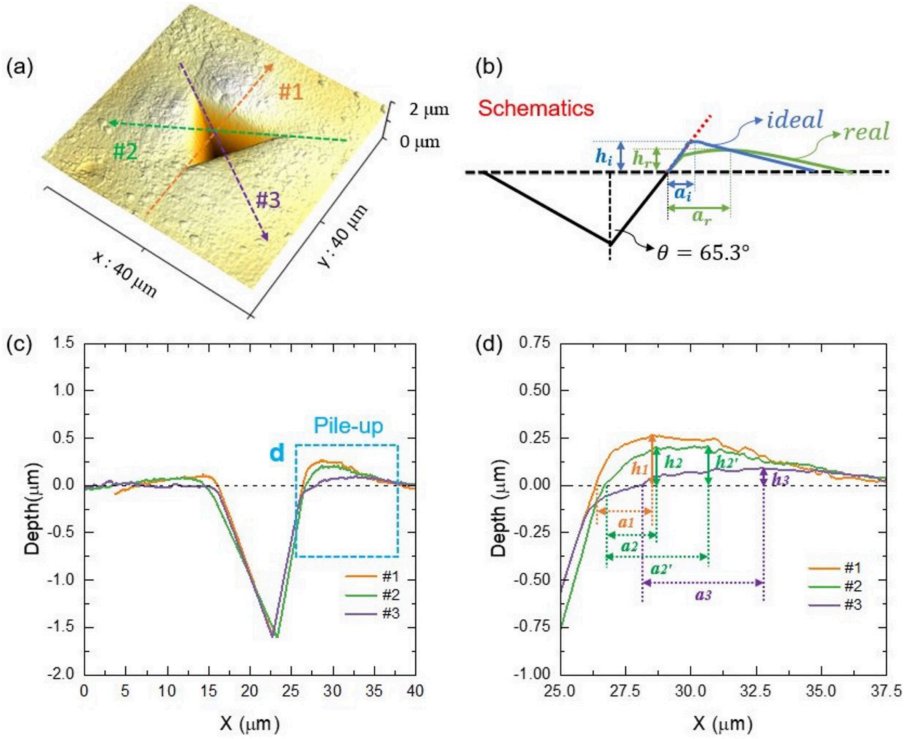

Figure 4. (a) An AFM image of an indentation imprint on $Ni_{80}Cr_{20}$ displays apparent pile-ups; (b) The surface profiles of ideal and real pile-up profiles are schematically shown to determine the contact periphery of the indenter (a_i) and height of pile-up (h_i); (c-d) The three surface profiles in (a) show a_i and h_i (i=1-3).

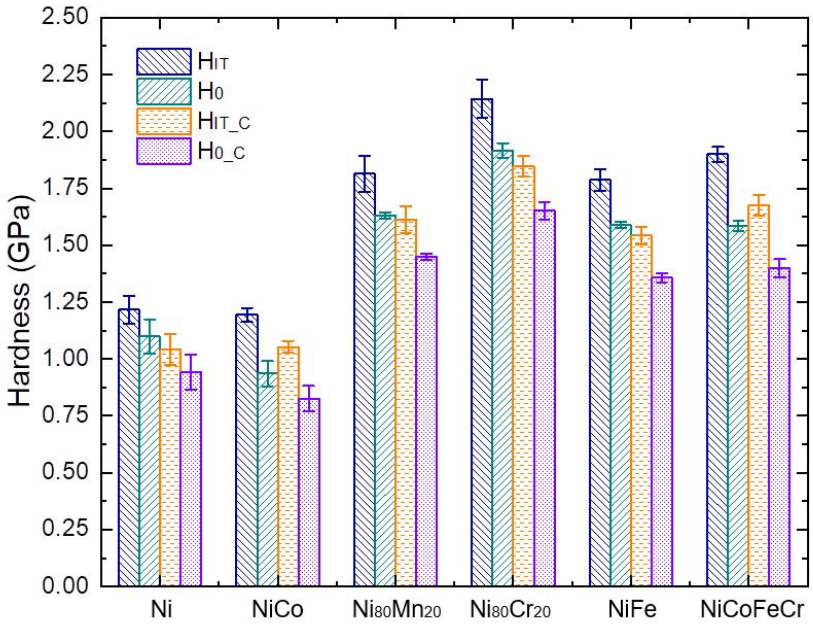

Figure 5. A summary of nanoindentation hardness at 2 μm (H_{IT}), macro-hardness (H_0) from Nix-Gao model, pile-up corrected H_{IT} (H_{IT_C}), and pile-up corrected H_0 (H_{0_C}).

3.2 Geometrically necessary dislocations and statistically stored dislocations in CSAs

For ductile materials such as Ni and CSAs in this study, the plastic deformation during indentation is carried by dislocations. The increase in dislocation density leads to higher flow stress of the materials. During nanoindentation, two types of dislocations are considered: geometrically necessary dislocations (GNDs) and statistically stored dislocations (SSDs) [55, 56]. The densities of GNDs (ρ_G) and SSDs (ρ_s) in Ni and CSAs are estimated to understand the different deformation behaviors of CSAs. The GND density is related to the strain gradient by compatibility requirements. The strain gradient has to be accommodated by a certain number of GNDs and Ma-Clarke model estimates the GND density as [57, 58]

$$\rho_G = \frac{4\gamma}{bh} \quad (5)$$

where γ refers to average shear strain, b represents Burgers vector, and h is indentation penetration depth. Accordingly, combined with Taylor relation, hardness is approximated by ρ_s and ρ_G [59],

$$H \approx \mu b[\rho_s + \rho_G]^{1/2} \quad (6)$$

where μ is shear modulus from nanoindentation; ρ_s is estimated from corrected hardness by $(H_{0\_C}/\mu b)^2$, which is constant and depth independent. On the other hand, ρ_G is depth dependent: At the depth of 2 μm, the corrected hardness, H_{IT_C} was used as H in Eqn. 6 and therefore ρ_G can be obtained at $h = 2\ \mu m$. ρ_s and ρ_G are summarized in Fig. 6. ρ_s is the largest in NiFe ($8.5 \times 10^{15}/m^2$), lower in $Ni_{80}Cr_{20}$ ($7.1 \times 10^{15}/m^2$), $Ni_{80}Mn_{20}$ ($6.2 \times 10^{15}/m^2$), and NiCoFeCr ($6.1 \times 10^{15}/m^2$), and lowest in Ni ($2.9 \times 10^{15}/m^2$) and NiCo ($2.4 \times 10^{15}/m^2$). The comparison of ρ_S and ρ_G shows that at the depth of 2 μm, ρ_S plays a more dominant contribution to hardness.

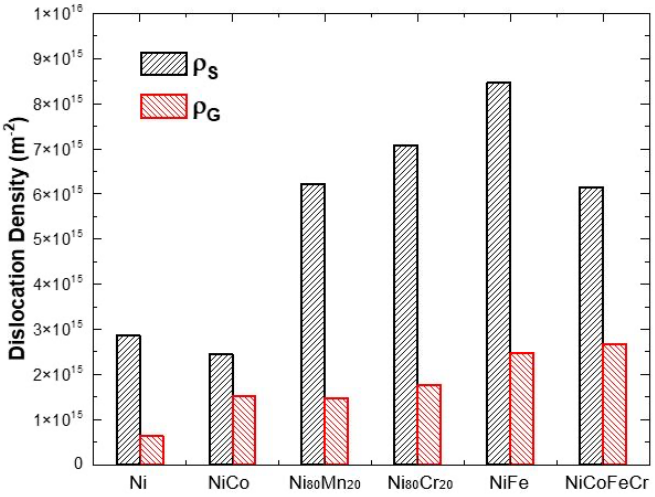

Figure 6. Densities of Statistically Stored Dislocations (SSD, ρ_S) and Geometrically Necessary Dislocations (GND, ρ_G) for Ni and CSAs calculated from the Ma-Clarke model.

As shown in Eqn. 5, ρ_G is depth dependent. With the known ρ_G at $h = 2\ \mu m$, the only unknown parameter, γ in Eqn. 5 can be obtained for all CSAs. Therefore, the indentation depth dependent

ρ_G for all CSAs is compared in Fig. 7. ρ_G decreases at a deeper penetration depth. ρ_G is the highest in NiCoFeCr, lower in NiFe and $Ni_{80}Cr_{20}$, and the lowest in Ni. NiCo and $Ni_{80}Mn_{20}$ have close ρ_G. This interesting observation can be reasoned as follows. It is assumed in the Nix-Gao model that the distribution of GNDs is constrained within the hemispherical shape underneath the indenter, as schematically shown in the inset of Fig. 7. If it is assumed that the total number of GNDs required to accommodate the compatibility requirements from indentation is the same for all samples, a higher ρ_G means a smaller volume accommodating GNDs. This implies that the migration of GNDs is easier in Ni, which allows a longer migration distance, but it is more difficult in CSAs. This is related to dislocation migration kinetics and SSD density. This assumption is consistent with the discovery by molecular dynamics simulation that dislocations underneath the indenter migrate slower in NiFe than in pure Ni [60]. More information on dislocation migration can be reflected by the activation volume of dislocations, which will be studied by nanoindentation strain rate jump tests in the following section.

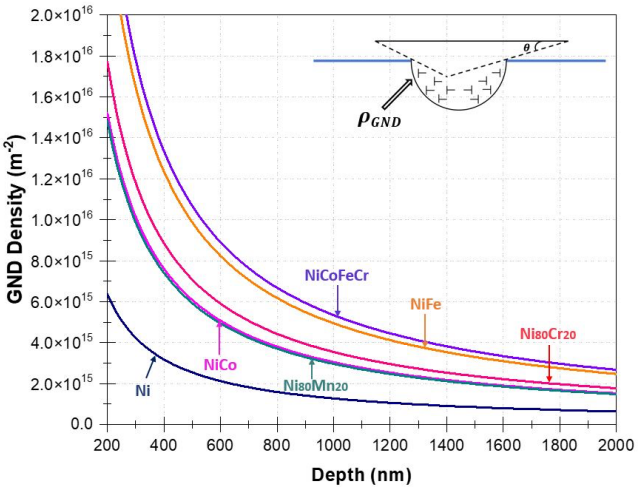

Figure 7. Depth dependence of GND density in Ni and CSAs. The inset schematically shows GNDs distribute within a hemispherical volume underneath an indenter.

3.3 Strain rate sensitivity and activation volume in CSAs

Strain rate sensitivity (m) and activation volume (V) are two key parameters that are useful for understanding the deformation kinetics [61, 62]. The activation volume is defined as the volume of a material involved in the process of overcoming the energy barrier. Here, the activation volume expresses the volume that is physically swept by a dislocation from a ground equilibrium state to an activated state after the deformation [63].

Nanoindentation strain rate jump tests, which abruptly vary the strain rate during indentation, have been demonstrated to be a reliable method for strain rate sensitivity by Maier *et al.* [64]. The strain rate for indentation ($\dot{\varepsilon}_i$) was defined by Lucas and Oliver [65] as

$$\dot{\varepsilon}_i = \frac{\dot{h}}{h} = \frac{1}{2}\left(\frac{\dot{P}}{P} - \frac{\dot{H}}{H}\right) \qquad (7)$$

where h and $\dot{h}$ are instantaneous displacement and displacement rate of the indenter, P and $\dot{P}$ are the current load and loading rate, and $\dot{H}$ is the hardness change rate (unit: Pa/s). This method has been successfully used for ultrafine-grained and nano-grained metals where H is constant with

indentations depths larger than tens or hundreds of nanometers (i.e., $\dot{H}/H = 0$) [64]. In our Ni and CSAs, H keeps decreasing due to ISE *and* $\dot{H}/H$ is not negligible. Therefore, instead of using the conventional assumption of $\dot{H}/H = 0$ in literature, $\dot{H}/H$ is included in our calculation for indentation strain rate (Eqn. 7). Subsequently, the strain rate sensitivity of materials can be obtained with modified $\dot{\varepsilon}_i$. This technique was modified from CSM standard method, and several sudden changes in applied strain rates were conducted at several fixed indentation depths within one single test. Figure 8a shows one example in our tests, in which the method to identify the hardness before and after strain rate jumps is labeled. Three strain rates ($\dot{\varepsilon}$ = 0.05/s, 0.007/s, 0.001/s) are selected for jump tests and the base strain rate is 0.05/s. The strain rate sensitivity, m can be calculated by [64]

$$m = \frac{d(lnH)}{d(ln\dot{\varepsilon})} \quad (8)$$

Also, the activation volume, V can be calculated from m and H [64]

$$V = \frac{3\sqrt{3}\kappa T}{m \cdot H} \quad (9)$$

where κ is the Boltzmann constant and T is the absolute temperature. Six indents were performed on each sample for repeatability and the average was taken. The calculated m and corresponding V are summarized in Fig. 8. m is highest in NiCoFeCr (0.0088) and lowest in NiCo (0.0065). Overall, m increases with the increase in the number of elements. V shows an opposite trend with m. The pure Ni and NiCo show larger V of respective 162.5 and 173.1b^3 (b is Burgers vector). V in $Ni_{80}Mn_{20}$, $Ni_{80}Cr_{20}$, NiFe and NiCoFeCr are 96.7, 91.7, 91.3 and 82.4 b^3, respectively. The close value of V in Ni and NiCo suggests that the addition of Co into Ni doesn't change the dislocation kinetics significantly. In contrast, the addition of Fe, Cr and Mn affects dislocation migration significantly. The activation volumes in the range of 82.4 -173 b^3 indicate that the mechanisms with a small V of ~ 1 b^3, such as the kink-pair mechanism, are not dominant in our study. As a reference, in conventional FCC metals with large grain sizes, the forest dislocation interaction dominates the plastic deformation and the activation volume is ~100 -1000 b^3 [66, 67].

In CSAs, both multiple principal elements and forest dislocations contribute to activation volumes of dislocations. Laplanche *et al*. [68] have demonstrated that the inverse activation volumes of solid solution strengthening and forest hardening are additive, i.e., $1/V=1/V_{SS}+1/V_f$. For activation volume for solid solution strengthening, a dislocation in the random alloy responds to the presence of spatially varying concentrations by adopting a wavy shape characterized by wavelength and amplitude. The selection of characteristic waviness is one that minimizes the total dislocation energy by enabling the dislocation to reside in regions of favorable (energy-lowering) regions of concentration fluctuations at the expense of the line tension cost of the wavy shape. The solid solution strengthening effects will be discussed in the next section and here forest dislocations are our focus. The activation volume for forest hardening is associated with the activation area, which is defined by the area swept out by a dislocation segment with a length (l) over a distance (w) by overcoming energy barriers. The activation area and activation volume can be related by $V= bwl$ [69, 70]. It is assumed that the dislocation segment is pinned by two dislocation junctions and therefore the distance between two junctions (segment length l) is estimated by $\rho^{-1/2}$ for all CSAs as follows: Ni: 17 nm; NiCo: 16 nm; $Ni_{80}Cr_{20}$: 11 nm; $Ni_{80}Mn_{20}$: 11 nm; NiFe: 10 nm; NiCoFeCr, 11 nm. As a result, w is calculated as 7.5-11 nm, which is lower than l (10-17 nm). The lower w might be related to the local varying concentrations, which is beyond our focus here but deserve further investigations by atomistic simulations.

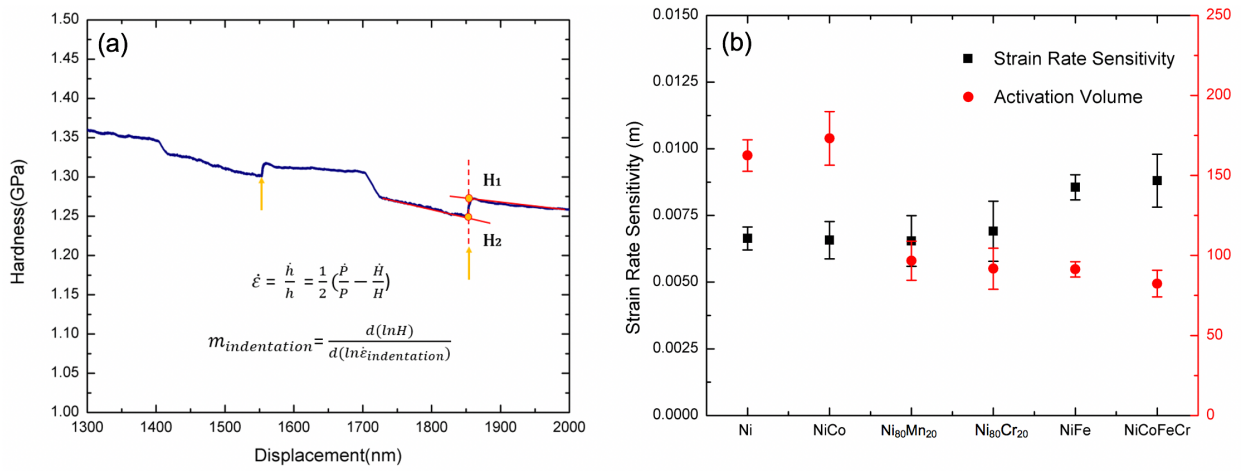

Figure 8. (a) Determination of strain rate sensitivity by considering the hardness change rate (unit: Pa/s) during nanoindentation strain rate jump tests. Nominal nanoindentation strain rates are 0.05/s, 0.007/s and 0.001/s. (b) The values of strain rate sensitivity and corresponding activation volume for Ni and CSAs.

3.4 Deformation mechanisms of CSAs under indentation

As discussed in Section 1, the deformation in CSAs can be described under the framework of conventional strengthening mechanisms. In our study on Ni-based CSAs, twinning isn't significant at room temperature, and grain boundary strengthening doesn't exist. Therefore, our discussion focuses on solid solution strengthening and forest hardening.

First, SFEs of Ni and CSAs are compared as SFE often determines the dislocation core structure and corresponding migration kinetics. As summarized in Table 1, the addition of alloying elements into Ni generally lowers SFE. The SFE decreases from 127 mJ/m^2 for pure Ni, to near or below 100 mJ/m^2 for CSAs. As chemical composition varies in CSAs beyond the dilute limit, SFE has a large variation depending on the local atomic environment: The local SFE can be very small and even negative at several sites even though the average SFE remains positive [71]. The negative SFE in FCC CSAs is caused by the energetic preference of hexagonal closed-packed stacking. Furthermore, SRO may also change SFE. For CrCoNi, first-principles calculation shows that intrinsic SFE can be tuned from -42.9 to 30 mJ/m^2 by adjusting SRO [72], which has also been confirmed by experiments [73]. In our study, SFE does not play a significant role in hardness. As shown in Table 1, a significant reduction in SFE from 127 mJ/m^2 in Ni to -10 mJ/m^2 in NiCo does not lead to a significant change in hardness; Also, NiFe and NiCoFeCr with distinct SFEs have a close hardness. Therefore, there is no obvious correlation between SFE and hardness in Ni-based CSAs at room temperature in this study. This observation is consistent with the finding that SFE is less important in CSAs when it is below 100 mJ/m^2 because the separation of two partial dislocations is larger than 10 *b* [74].

The hardness from nanoindentation reflects the flow stress, which includes solid solution strengthening and work hardening in our study. It is worth noting that hardness alone cannot be distinguished whether the strength is contributed by solid solution strengthening or work hardening. CSAs containing multiple principal elements have serious lattice distortion caused by a large atomic radius difference between different components, which is distinctive from that in pure metal and conventional alloys. The lattice distortion would affect both work hardening and solid solution strengthening.

(a) Work hardening: To understand the work hardening of CSAs during nanoindentation, hardness is compared to tensile properties (i.e., yield strength, σ_Y, and ultimate tensile strength, σ_{UTS}) of Ni, NiCo, NiFe, and NiCoFeCr, available in literature [11], as summarized in Table 1. The strength of CSAs, estimated by $H/3$ [38] lies in between σ_Y and σ_{UTS}. Furthermore, strain during nanoindentation is estimated based on the reported tensile stress-strain curves in literature [11] and the strains to reach $H/3$ for Ni, NiCo, NiFe, and NiCoFeCr are estimated as 15%, 7%, 16%, and 7%, respectively (Table 1). The representative strains for Ni, and NiCoFeCr are close to the representative strain range between 8% and 10% suggested by Tabor [20] for ductile and work-hardenable metals. Ni and NiFe show higher representative strain of ~15%, indicating they are more work hardenable during indentation. Note that tensile properties in [11] were obtained from polycrystalline CSAs with a grain size of 24-85 μm and the grain boundary strengthening is not considered here.

Table 1. *A summary of stacking fault energies (SFEs), yield and ultimate tensile strengths (σ_Y and σ_{UTS}) and estimated strain during nanoindentation for Ni and CSAs.*

Sample	**SFE (mJ/m^2)**	**σ_Y (MPa)**	**σ_{UTS} (MPa)**	**σ (=H/3) (MPa)**	**Estimated strain during indentation (using tensile data in [11])**
Ni	127 [18]	94 [11]	348 [11]	314	15%
NiCo	-10 [18]	110 [11]	542 [11]	275	7%
$Ni_{80}Mn_{20}$	--	--	--	483	--
$Ni_{80}Cr_{20}$	101 [75]	--	--	550	--
NiFe	105 [18]	188 [11]	512 [11]	452	16%
NiCoFeCr	-22 [18]; 20 [76]; 34.3 [77]	271 [11]	711 [11]	467	7%

(b) Solid solution strengthening: Compared to work hardening, solid solution strengthening is the main cause of the exceptional mechanical properties of HEAs [78] and many strengthening models have been developed, considering dislocation interactions with the random local concentration fluctuations. Starting from the solid solution strengthening models for binary systems by Fleischer [79] and Labush [80], the theory has been extended to alloys with multiple principal elements [81, 82]. For FCC CSAs, Varvenne *et al*. [74] recently proposed a predictive model in which each element in CSAs is considered as a solute embedded in an effective matrix of surrounding atoms. One advantage of this model is that it does not include any adjustable parameters and allows all model parameters to be computed by experiments or simulations. In addition, the predictive model includes the temperature-, and strain-rate dependence of the strength of FCC CSAs, which anticipates future studies on thermal and strain rate effects. The details of model implementations are as follows.

In this model, lattice distortion plays a central role in strengthening in CSAs [83]. The average misfit volume of n^{th} element ($\Delta\bar{V}_n$) is calculated from $\Delta\bar{V}_n = V_n - \bar{V}$, with $\bar{V} = \sum C_n V_n$ and V_n is

atomic volume, measured from atomistic simulation or experiments. Since each element has its specific atomic size, severe lattice distortion can occur in CSAs. The lattice distortion (δ) (atomic-size difference) can be estimated by [84]

$$\delta = \sqrt{\sum_{i=i}^{N} c_i\left(1 - r_i / \sum_{j=1}^{N} c_j r_j\right)}^2 \qquad (10)$$

where N is the number of the components in an alloy system, c_i is the atomic percentage of the ith component, $\sum_{j=1}^{N} c_j r_j$ is the average atomic radius, and r_i is the atomic radius. To explicitly show the influence of lattice distortion (δ) in the solid solution strengthening, the key solute quantity ($\sum C_n \Delta \bar{V}_n^2$) in the model from Varvenne *et al.* was replaced by $9\bar{V}^2\delta^2$ [74]. Therefore, the solid solution strengthening can be calculated as [74]

$$\sigma_{SS}(T, \dot{\varepsilon}) = M\tau_{y0}\exp\left(-\frac{1}{0.51}\frac{kT}{\Delta E_b}\ln\frac{\dot{\varepsilon_0}}{\dot{\varepsilon}}\right) \qquad (11)$$

where

$$\Delta E_b = 0.274\alpha^{\frac{1}{3}}\mu b^3\left(\frac{1+v}{1-v}\right)^{\frac{2}{3}} f_2(w_c) \times \left(\frac{9\bar{V}^2\delta^2}{b^6}\right)^{\frac{1}{3}} \qquad (12)$$

$$\tau_{y0} = 0.051\alpha^{-\frac{1}{3}}\mu\left(\frac{1+v}{1-v}\right)^{\frac{4}{3}} f_1(w_c) \times \left(\frac{9\bar{V}^2\delta^2}{b^6}\right)^{\frac{2}{3}} \qquad (13)$$

where M is Taylor factor, 3.06; $\dot{\varepsilon}$ is strain rate, 0.05/s for nanoindentation; μ is shear modulus, estimated from nanoindentation by $\mu = E/2(1+v)$. The rest parameters are the same as [74]: α is dislocation line tension parameter, 0.123; $f_1(w_c) = 0.35$; $f_2(w_c) = 5.70$; $\dot{\varepsilon_0}$ is the reference strain rate, 10000/s; T = 293 K. Two different sets of atomic radii are selected for δ: one is by using Goldschmidt radius (δ_G); The other is by using atomic radius in the relaxed structure from atomistic simulation and experiments (δ_{rlx}), which are summarized in Table 2. The atomic radii for δ_{rlx} were calculated from the volume of components [74].

As shown in Table 2, The assumption that the atomic size is intrinsic to the element (e.g., Goldschmidt radius) is not applicable for CSAs in this study: δ_G and corresponding σ_{SS} for $Ni_{80}Mn_{20}$ are unrealistically high due to the distinct Goldschmidt radius for Mn, while σ_{SS} for $Ni_{80}Cr_{20}$, NiFe and NiCoFeCr are significantly lower than the experimental results. $\sigma_{SS}(\delta_{rlx})$ demonstrates that NiCo has negligible σ_{SS}, similar to pure Ni. The hardness values of Ni and NiCo are also close, which are obviously lower than the rest of the CSAs. From the ratio of σ_{SS}/σ, NiCoFeCr and $Ni_{80}Mn_{20}$ exhibit a higher portion of solid solution strengthening than the rest of the CSAs. Results for $Ni_{80}Mn_{20}$ and $Ni_{80}Cr_{20}$ are not compared with literature as these two CSAs are less explored. However, based on our study, they are promising as they demonstrated high hardness (from nanoindentation) and σ_{SS} (Table 1). This suggests that the selection of component elements in CSAs is critical, and more efforts should be devoted to understanding element-specific deformation mechanisms in CSAs for better property combinations.

Table 2. *Solid Solution Strengthening in Ni and CSAs.*

Sample	***E* (GPa) Nanoindentation**	**σ (=H/3) (MPa)**	**δ_G ***	**$\sigma_{SS}(\delta_G)$ (MPa)**	**δ_{rlx} ****	**$\sigma_{SS}(\delta_{rlx})$ (MPa)**	**$\sigma_{SS}(\delta_{rlx})/\sigma$**
Ni	184±4	314	0.0000	0.0	0.0000	0.0	0.00

NiCo	174±6	275	0.0040	4.0	0.0027	1.2	0.00
$Ni_{80}Mn_{20}$	191±5	483	0.0425	457.2	0.0191	130.1	0.27
$Ni_{80}Cr_{20}$	205±3	550	0.0096	41.5	0.0155	98.5	0.18
NiFe	153±5	452	0.0119	33.5	0.0167	64.0	0.14
NiCoFeCr	186±2	467	0.0102	47.7	0.0167	109.6	0.24

[*] Goldschmidt radius: Ni: 1.25 Å; Co: 1.26 Å; Mn: 1.12 Å; Cr: 1.28 Å; Fe: 1.28 Å.

[**] Atomic radius calculated from atomistic simulations and experiments [74]: Ni: 1.25 Å; Co: 1.25 Å; Mn: 1.31 Å; Cr: 1.29 Å; Fe: 1.29 Å

4. Conclusions

A procedure for nanoindentation and nanoindentation strain rate jump tests and data analysis/correction has been developed for exploring Ni-based CSAs. Unique single-crystal FCC Ni, NiCo, $Ni_{80}Cr_{20}$, NiFe and NiCoFeCr, and coarse-grained $Ni_{80}Mn_{20}$ have been compared to understand the strengthening mechanisms, especially for the less explored binary alloys such as $Ni_{80}Cr_{20}$ and $Ni_{80}Mn_{20}$. A data set, including hardness, elastic modulus, strain rate sensitivity, and activation volume, is provided for Ni-based CSAs. Major conclusions are listed as follows.

- The type of alloying elements is more critical than the number of elements in strengthening: Co does not provide strengthening in Ni, while Cr, Mn, and Fe are effective strengthening elements. Cr is the most effective among all the 3*d* transition metal elements. The alloying in CSAs simultaneously increases the densities of statistically stored dislocations and geometrically necessary dislocations.
- Pile-ups and indentation size effects are significant in Ni-based CSAs and a correction procedure for accurate hardness was developed. It is suggested that the measured height, h_i instead of contact periphery, a_i should be used to estimate pile-ups for Ni-based CSAs.
- A data set of activation volumes of Ni-based CSA is provided from nanoindentation strain rate jump tests: Ni and Co are similar with a low activation volume for dislocations, while the rest have higher activation volumes. The data are consistent with hardness and dislocation analysis. One special consideration of ISE is included in analysis, i.e., the hardness change rate (unit: Pa/s) is not negligible for strain rate calculation for Ni-based CSAs with strong ISE.
- That lattice distortion from atomic-size difference plays a central role in strengthening, including solid solution strengthening and work hardening, while the SFE is not critical in our study. The utilization of the solid solution strengthening model developed by Varvenne *et al.* shows that atomic-size difference should be calculated based on the appropriate atomic radius in a relaxed structure from experiments/simulations, instead of the intrinsic Goldschmidt radius.

5. Acknowledgments

L.Y. and Y.C. acknowledge financial support by NSF-CMMI 1728554. Y.Z. W.J.W and H.B. were supported as part of Energy Dissipation to Defect Evolution (EDDE), an Energy Frontier Research Center funded by the U.S. Department of Energy, Office of Science, Basic Energy Sciences, under contract number DE-AC05-00OR22725. This work was performed in part at the Analytical Instrumentation Facility (AIF) at North Carolina State University, which is supported

by the State of North Carolina and the National Science Foundation (award number ECCS-2025064). L.Y. and Y.C. also acknowledge the discussion and support from Prof. Christopher Evans.

6. References

[1] J.W. Yeh, S.K. Chen, S.J. Lin, J.Y. Gan, T.S. Chin, T.T. Shun, C.H. Tsau, S.Y. Chang, Nanostructured high-entropy alloys with multiple principal elements: novel alloy design concepts and outcomes, Advanced Engineering Materials 6(5) (2004) 299-303.
[2] B. Cantor, I. Chang, P. Knight, A. Vincent, Microstructural development in equiatomic multicomponent alloys, Materials Science and Engineering: A 375 (2004) 213-218.
[3] Z. Li, S. Zhao, R.O. Ritchie, M.A. Meyers, Mechanical properties of high-entropy alloys with emphasis on face-centered cubic alloys, Progress in Materials Science 102 (2019) 296-345.
[4] E.P. George, W. Curtin, C.C. Tasan, High entropy alloys: A focused review of mechanical properties and deformation mechanisms, Acta Materialia 188 (2020) 435-474.
[5] Y. Shang, J. Brechtl, C. Pistidda, P.K. Liaw, Mechanical behavior of high-entropy alloys: A review, High-Entropy Materials: Theory, Experiments, and Applications (2021) 435-522.
[6] Y. Zhang, Y.N. Osetsky, W.J. Weber, Tunable Chemical Disorder in Concentrated Alloys: Defect Physics and Radiation Performance, Chemical Reviews 122(1) (2022) 789-829.
[7] O. El-Atwani, N. Li, M. Li, A. Devaraj, J. Baldwin, M.M. Schneider, D. Sobieraj, J.S. Wróbel, D. Nguyen-Manh, S.A. Maloy, Outstanding radiation resistance of tungsten-based high-entropy alloys, Science advances 5(3) (2019) eaav2002.
[8] Y. Zhang, G.M. Stocks, K. Jin, C. Lu, H. Bei, B.C. Sales, L. Wang, L.K. Béland, R.E. Stoller, G.D. Samolyuk, Influence of chemical disorder on energy dissipation and defect evolution in concentrated solid solution alloys, Nature communications 6(1) (2015) 1-9.
[9] D.B. Miracle, O.N. Senkov, A critical review of high entropy alloys and related concepts, Acta Materialia 122 (2017) 448-511.
[10] E.P. George, D. Raabe, R.O. Ritchie, High-entropy alloys, Nature Reviews Materials 4(8) (2019) 515-534.
[11] Z. Wu, H. Bei, G.M. Pharr, E.P. George, Temperature dependence of the mechanical properties of equiatomic solid solution alloys with face-centered cubic crystal structures, Acta Materialia 81 (2014) 428-441.
[12] H.S. Oh, S.J. Kim, K. Odbadrakh, W.H. Ryu, K.N. Yoon, S. Mu, F. Körmann, Y. Ikeda, C.C. Tasan, D. Raabe, Engineering atomic-level complexity in high-entropy and complex concentrated alloys, Nature communications 10(1) (2019) 1-8.
[13] Y. Zhang, X. Wang, Y.N. Osetsky, Y. Tong, R. Harrison, S.E. Donnelly, D. Chen, Y. Wang, H. Bei, B.C. Sales, Effects of 3d electron configurations on helium bubble formation and void swelling in concentrated solid-solution alloys, Acta Materialia 181 (2019) 519-529.
[14] Z. Zhang, M. Mao, J. Wang, B. Gludovatz, Z. Zhang, S.X. Mao, E.P. George, Q. Yu, R.O. Ritchie, Nanoscale origins of the damage tolerance of the high-entropy alloy CrMnFeCoNi, Nature communications 6(1) (2015) 1-6.
[15] G. Laplanche, A. Kostka, C. Reinhart, J. Hunfeld, G. Eggeler, E. George, Reasons for the superior mechanical properties of medium-entropy CrCoNi compared to high-entropy CrMnFeCoNi, Acta Materialia 128 (2017) 292-303.
[16] J. Zhang, W.-Z. Han, Oxygen solutes induced anomalous hardening, toughening and embrittlement in body-centered cubic vanadium, Acta Materialia 196 (2020) 122-132.

[17] L. Qi, Effects of electronic structures on mechanical properties of transition metals and alloys, Computational Materials Science 163 (2019) 11-16.
[18] S. Zhao, G.M. Stocks, Y. Zhang, Stacking fault energies of face-centered cubic concentrated solid solution alloys, Acta Materialia 134 (2017) 334-345.
[19] C. Wen, C. Wang, Y. Zhang, S. Antonov, D. Xue, T. Lookman, Y. Su, Modeling solid solution strengthening in high entropy alloys using machine learning, Acta Materialia 212 (2021) 116917.
[20] D. Tabor, The hardness of metals, Oxford university press2000.
[21] J. Pethicai, R. Hutchings, W.C. Oliver, Hardness measurement at penetration depths as small as 20 nm, Philosophical Magazine A 48(4) (1983) 593-606.
[22] W.C. Oliver, G.M. Pharr, An improved technique for determining hardness and elastic modulus using load and displacement sensing indentation experiments, Journal of materials research 7(6) (1992) 1564-1583.
[23] Y. Chen, E. Hintsala, N. Li, B.R. Becker, J.Y. Cheng, B. Nowakowski, J. Weaver, D. Stauffer, N.A. Mara, High-throughput nanomechanical screening of phase-specific and temperature-dependent hardness in Al x FeCrNiMn high-entropy alloys, Jom 71(10) (2019) 3368-3377.
[24] Y. Chen, Y. Liu, C. Sun, K. Yu, M. Song, H. Wang, X. Zhang, Microstructure and strengthening mechanisms in Cu/Fe multilayers, Acta Materialia 60(18) (2012) 6312-6321.
[25] G. Pharr, W. Oliver, Measurement of thin film mechanical properties using nanoindentation, Mrs Bulletin 17(7) (1992) 28-33.
[26] R. Saha, W.D. Nix, Effects of the substrate on the determination of thin film mechanical properties by nanoindentation, Acta materialia 50(1) (2002) 23-38.
[27] K. Jin, C. Lu, L. Wang, J. Qu, W. Weber, Y. Zhang, H. Bei, Effects of compositional complexity on the ion-irradiation induced swelling and hardening in Ni-containing equiatomic alloys, Scripta Materialia 119 (2016) 65-70.
[28] K. Jin, Y. Xia, M. Crespillo, H. Xue, Y. Zhang, Y. Gao, H. Bei, Quantifying early stage irradiation damage from nanoindentation pop-in tests, Scripta Materialia 157 (2018) 49-53.
[29] P. Hosemann, D. Kiener, Y. Wang, S.A. Maloy, Issues to consider using nano indentation on shallow ion beam irradiated materials, Journal of Nuclear Materials 425(1-3) (2012) 136-139.
[30] X. Zhang, K. Hattar, Y. Chen, L. Shao, J. Li, C. Sun, K. Yu, N. Li, M.L. Taheri, H. Wang, Radiation damage in nanostructured materials, Progress in Materials Science 96 (2018) 217-321.
[31] Y. Chen, Y. Liu, E. Fu, C. Sun, K. Yu, M. Song, J. Li, Y. Wang, H. Wang, X. Zhang, Unusual size-dependent strengthening mechanisms in helium ion-irradiated immiscible coherent Cu/Co nanolayers, Acta Materialia 84 (2015) 393-404.
[32] D. Lucca, K. Herrmann, M. Klopfstein, Nanoindentation: Measuring methods and applications, CIRP annals 59(2) (2010) 803-819.
[33] C.A. Schuh, Nanoindentation studies of materials, Materials today 9(5) (2006) 32-40.
[34] X. Li, B. Bhushan, A review of nanoindentation continuous stiffness measurement technique and its applications, Materials characterization 48(1) (2002) 11-36.
[35] P. Zhang, S. Li, Z. Zhang, General relationship between strength and hardness, Materials Science and Engineering: A 529 (2011) 62-73.
[36] Y.-T. Cheng, C.-M. Cheng, Scaling, dimensional analysis, and indentation measurements, Materials Science and Engineering: R: Reports 44(4-5) (2004) 91-149.
[37] D. Tabor, The hardness and strength of metals, J. Inst. Metals 79 (1951) 1.
[38] X. Fan, R. Qu, Z. Zhang, Relation Between Strength and Hardness of High-Entropy Alloys, Acta Metallurgica Sinica (English Letters) (2021) 1-22.

[39] J. Gale, A. Achuthan, The effect of work-hardening and pile-up on nanoindentation measurements, Journal of materials science 49(14) (2014) 5066-5075.
[40] C. Lu, K. Jin, L.K. Béland, F. Zhang, T. Yang, L. Qiao, Y. Zhang, H. Bei, H.M. Christen, R.E. Stoller, Direct observation of defect range and evolution in ion-irradiated single crystalline Ni and Ni binary alloys, Scientific reports 6(1) (2016) 1-10.
[41] T.-n. Yang, C. Lu, G. Velisa, K. Jin, P. Xiu, M.L. Crespillo, Y. Zhang, H. Bei, L. Wang, Effect of alloying elements on defect evolution in Ni-20X binary alloys, Acta Materialia 151 (2018) 159-168.
[42] C. Lu, T. Yang, K. Jin, N. Gao, P. Xiu, Y. Zhang, F. Gao, H. Bei, W.J. Weber, K. Sun, Radiation-induced segregation on defect clusters in single-phase concentrated solid-solution alloys, Acta Materialia 127 (2017) 98-107.
[43] T.B. Massalski, H. Okamoto, P. Subramanian, L. Kacprzak, W.W. Scott, Binary alloy phase diagrams, American society for metals Metals Park, OH1986.
[44] D. Nečas, P. Klapetek, Gwyddion: an open-source software for SPM data analysis, Open Physics 10(1) (2012) 181-188.
[45] X. Ma, W. Higgins, Z. Liang, D. Zhao, G.M. Pharr, K.Y. Xie, Exploring the origins of the indentation size effect at submicron scales, Proceedings of the National Academy of Sciences 118(30) (2021) e2025657118.
[46] M. Rester, C. Motz, R. Pippan, Microstructural investigation of the volume beneath nanoindentations in copper, Acta Materialia 55(19) (2007) 6427-6435.
[47] N. Tymiak, D. Kramer, D. Bahr, T. Wyrobek, W.W. Gerberich, Plastic strain and strain gradients at very small indentation depths, Acta Materialia 49(6) (2001) 1021-1034.
[48] W.D. Nix, H. Gao, Indentation size effects in crystalline materials: a law for strain gradient plasticity, Journal of the Mechanics and Physics of Solids 46(3) (1998) 411-425.
[49] C. Heintze, F. Bergner, S. Akhmadaliev, E. Altstadt, Ion irradiation combined with nanoindentation as a screening test procedure for irradiation hardening, Journal of Nuclear Materials 472 (2016) 196-205.
[50] M. Dao, N.v. Chollacoop, K. Van Vliet, T. Venkatesh, S. Suresh, Computational modeling of the forward and reverse problems in instrumented sharp indentation, Acta materialia 49(19) (2001) 3899-3918.
[51] P. Zhu, Y. Zhao, S. Agarwal, J. Hay, J. Henry, S. Zinkle, Challenges to accurate evaluation of bulk hardness from nanoindentation testing at low indent depths, Available at SSRN 3793936.
[52] K. Kese, Z.-C. Li, B. Bergman, Method to account for true contact area in soda-lime glass during nanoindentation with the Berkovich tip, Materials Science and Engineering: A 404(1-2) (2005) 1-8.
[53] K. Kese, Z.-C. Li, Semi-ellipse method for accounting for the pile-up contact area during nanoindentation with the Berkovich indenter, Scripta materialia 55(8) (2006) 699-702.
[54] K. Jin, Y. Gao, H. Bei, Intrinsic properties and strengthening mechanism of monocrystalline Ni-containing ternary concentrated solid solutions, Materials Science and Engineering: A 695 (2017) 74-79.
[55] K. Durst, B. Backes, M. Göken, Indentation size effect in metallic materials: Correcting for the size of the plastic zone, Scripta Materialia 52(11) (2005) 1093-1097.
[56] B. Backes, Y. Huang, M. Göken, K. Durst, The correlation between the internal material length scale and the microstructure in nanoindentation experiments and simulations using the conventional mechanism-based strain gradient plasticity theory, journal of Materials Research 24(3) (2009) 1197-1207.

[57] Q. Ma, D.R. Clarke, Size dependent hardness of silver single crystals, Journal of Materials Research 10(4) (1995) 853-863.
[58] M. Ashby, The deformation of plastically non-homogeneous materials, The Philosophical Magazine: A Journal of Theoretical Experimental and Applied Physics 21(170) (1970) 399-424.
[59] Z. Zong, J. Lou, O. Adewoye, A. Elmustafa, F. Hammad, W. Soboyejo, Indentation size effects in the nano-and micro-hardness of fcc single crystal metals, Materials Science and Engineering: A 434(1-2) (2006) 178-187.
[60] L. Kurpaska, F. Dominguez-Gutierrez, Y. Zhang, K. Mulewska, H. Bei, W. Weber, A. Kosińska, W. Chrominski, I. Jozwik, R. Alvarez-Donado, Effects of Fe atoms on hardening of a nickel matrix: Nanoindentation experiments and atom-scale numerical modeling, Materials & Design 217 (2022) 110639.
[61] Q. Wei, S. Cheng, K. Ramesh, E. Ma, Effect of nanocrystalline and ultrafine grain sizes on the strain rate sensitivity and activation volume: fcc versus bcc metals, Materials Science and Engineering: A 381(1-2) (2004) 71-79.
[62] M. Tang, L. Kubin, G. Canova, Dislocation mobility and the mechanical response of bcc single crystals: a mesoscopic approach, Acta Materialia 46(9) (1998) 3221-3235.
[63] A. Sarkar, J. Chakravartty, Activation volume and density of mobile dislocations in plastically deforming Zr-1pctSn-1pctNb-0.1 pctFe alloy, Metallurgical and Materials Transactions A 46(12) (2015) 5638-5643.
[64] V. Maier, K. Durst, J. Mueller, B. Backes, H.W. Höppel, M. Göken, Nanoindentation strain-rate jump tests for determining the local strain-rate sensitivity in nanocrystalline Ni and ultrafine-grained Al, Journal of materials research 26(11) (2011) 1421-1430.
[65] B. Lucas, W. Oliver, Indentation power-law creep of high-purity indium, Metallurgical and materials Transactions A 30(3) (1999) 601-610.
[66] R.J. Asaro, S. Suresh, Mechanistic models for the activation volume and rate sensitivity in metals with nanocrystalline grains and nano-scale twins, Acta Materialia 53(12) (2005) 3369-3382.
[67] F. Dalla Torre, P. Spätig, R. Schäublin, M. Victoria, Deformation behaviour and microstructure of nanocrystalline electrodeposited and high pressure torsioned nickel, Acta Materialia 53(8) (2005) 2337-2349.
[68] G. Laplanche, J. Bonneville, C. Varvenne, W. Curtin, E.P. George, Thermal activation parameters of plastic flow reveal deformation mechanisms in the CrMnFeCoNi high-entropy alloy, Acta Materialia 143 (2018) 257-264.
[69] S. Gangireddy, B. Gwalani, R.S. Mishra, Grain size dependence of strain rate sensitivity in a single phase FCC high entropy alloy Al0. 3CoCrFeNi, Materials Science and Engineering: A 736 (2018) 344-348.
[70] J.W. Cahn, F. Nabarro, Thermal activation under shear, Philosophical Magazine A 81(5) (2001) 1409-1426.
[71] T.M. Smith, M.S. Hooshmand, B.D. Esser, F. Otto, D.W. McComb, E.P. George, M. Ghazisaeidi, M.J. Mills, Atomic-scale characterization and modeling of 60 dislocations in a high-entropy alloy, Acta Materialia 110 (2016) 352-363.
[72] J. Ding, Q. Yu, M. Asta, R.O. Ritchie, Tunable stacking fault energies by tailoring local chemical order in CrCoNi medium-entropy alloys, Proceedings of the National Academy of Sciences 115(36) (2018) 8919-8924.
[73] R. Zhang, S. Zhao, J. Ding, Y. Chong, T. Jia, C. Ophus, M. Asta, R.O. Ritchie, A.M. Minor, Short-range order and its impact on the CrCoNi medium-entropy alloy, Nature 581(7808) (2020) 283-287.

[74] C. Varvenne, A. Luque, W.A. Curtin, Theory of strengthening in fcc high entropy alloys, Acta Materialia 118 (2016) 164-176.
[75] M.S. Dodaran, S. Guo, M.M. Khonsari, N. Shamsaei, S. Shao, A theoretical calculation of stacking fault energy of Ni alloys: The effects of temperature and composition, Computational Materials Science 191 (2021) 110326.
[76] S. Huang, W. Li, S. Lu, F. Tian, J. Shen, E. Holmström, L. Vitos, Temperature dependent stacking fault energy of FeCrCoNiMn high entropy alloy, Scripta Materialia 108 (2015) 44-47.
[77] A. Zaddach, C. Niu, C. Koch, D. Irving, Mechanical properties and stacking fault energies of NiFeCrCoMn high-entropy alloy, Jom 65(12) (2013) 1780-1789.
[78] I. Toda-Caraballo, P.E. Rivera-Díaz-del-Castillo, Modelling solid solution hardening in high entropy alloys, Acta Materialia 85 (2015) 14-23.
[79] R.L. Fleischer, Substitutional solution hardening, Acta metallurgica 11(3) (1963) 203-209.
[80] R. Labusch, G. Grange, J. Ahearn, P. Haasen, Rate processes in plastic deformation of materials, Proceedings from the John E. Dorn Symposium, JCM Li and AK Muknergee, Ed., ASM Handbook, American Society for Metals, 1975.
[81] L. Gypen, A. Deruyttere, Multi-component solid solution hardening, Journal of materials science 12(5) (1977) 1028-1033.
[82] I. Toda-Caraballo, A general formulation for solid solution hardening effect in multicomponent alloys, Scripta Materialia 127 (2017) 113-117.
[83] R. Mishra, N. Kumar, M. Komarasamy, Lattice strain framework for plastic deformation in complex concentrated alloys including high entropy alloys, Materials Science and Technology 31(10) (2015) 1259-1263.
[84] Y. Zhang, Y.J. Zhou, J.P. Lin, G.L. Chen, P.K. Liaw, Solid-solution phase formation rules for multi-component alloys, Advanced engineering materials 10(6) (2008) 534-538.